IEEE Access
Multidisciplinary | Rapid Review | Open Access Journal

Received March 17, 2020, accepted March 29, 2020, date of publication April 3, 2020, date of current version May 4, 2020.

Digital Object Identifier 10.1109/ACCESS.2020.2985533

ISAR Imaging of Nonuniformly Rotating Targets With Low SNR Based on Third Order Autocorrelation Function

YANYAN LI[1], JIANCHENG ZHANG[2], JIBIN ZHENG[2], (Member, IEEE), JINPING NIU[1], YAN ZHOU[1], (Member, IEEE), AND NA MENG[1]

[1]School of Information Science and Technology, Northwest University, Xi'an 710127, China
[2]National Laboratory of Radar Signal Processing, Xidian University, Xi'an 710071, China

Corresponding authors: Yanyan Li (liyanyan_xd@163.com) and Jibin Zheng (jibin_zheng@sina.cn)

This work was supported in part by the National Natural Science Foundation of China under Grant 61901372, Grant 61901371, and Grant 61501372, in part by the Education Department of Shaanxi Province Natural Science Foundation under Grant 18JK0788 and Grant 18JK0777, and in part by the International Cooperation Foundation of Shaanxi Province under Grant 2019KW-012.

ABSTRACT This paper focuses on the inverse synthetic aperture radar (ISAR) imaging of nonuniformly rotating targets under low signal-to-noise ratio (SNR) environment, and an effective ISAR imaging algorithm based on a novel parameter estimation method is proposed. For nonuniformly rotating targets, the received signals in a range cell can be modeled as multicomponent cubic phase signals (CPSs) after the migration compensation and translation-induced phase error correction. For the CPS model, the chirp rate (CR) and quadratic chirp rate (QCR) will induce image defocus. To estimate the CR and QCR of CPS, a novel parameter method is presented. The basic idea of this method is to design a third order autocorrelation function (TOAF) which enable coherent accumulation of the signal energy in both of the time and lag-time domain. Compared with several state-of-the-art algorithms, the proposed method has a significant anti-noise performance improvement, while offering a proper computational complexity. The effectiveness and the superiority of the proposed ISAR imaging algorithm have been demonstrated through several simulation results.

INDEX TERMS Inverse synthetic aperture radar (ISAR), nonuniformly rotating target, third order autocorrelation function (TOAF), cubic phase signal (CPS), low signal-to-noise ratio (SNR) environment.

I. INTRODUCTION

Inverse synthetic aperture radar (ISAR) has been researched widely in the past several decades [1]–[5] since it is a useful technique to recognize non-cooperative targets [6], [7]. For targets whose Doppler frequency shift is constant during the imaging time, the range-Doppler (RD) ISAR imaging algorithm [2] is a powerful approach. Unfortunately, in realistic application, the targets are always maneuverable, and the Doppler frequency is time varying. As a result, the RD method will become invalid, and this problem motivates the study about the range instantaneous Doppler (RID) technique [8], [9].

To reconstruct a well-focused RID image, for the slowly maneuverable targets, the received signals in a range bin are modeled as multicomponent linear frequency modulated (LFM) signals after the migration compensation and translation-induced phase error correction [8]. Several ISAR imaging algorithms based on the parameter estimation methods for LFM signals have been presented [10]–[14]. However, for nonuniformly rotating targets with severe maneuverability, such as the fluctuating ship in the rough sea [15] and highly maneuvering aircraft [16], the LFM signal model will be unsuitable and the targets' echoes have to be modeled as cubic phase signals (CPSs), which has been validated by the real radar data and theoretical analysis [17].

For the CPS model, the chirp rate (CR) and quadratic chirp rate (QCR) are identified as the causes of image defocus in ISAR imaging. Thereby, the estimation of CR and QCR is an important step to reconstruct a high quality ISAR image, and several successful algorithms have been proposed. These

The associate editor coordinating the review of this manuscript and approving it for publication was Mauro Gaggero.

algorithms can be generally listed into two categories: linear algorithms [18], [19] and nonlinear algorithms [20]–[29].

The linear algorithms, such as maximum likelihood (ML) [18] and the modified discrete chirp Fourier transform (MDCFT) [19] can obtain good anti-noise performance, but their computational complexity is very high due to the parameter searching procedure in the implementations. To solve this problem, nonlinear algorithms are focused on. The cubic phase function (CPF) [20], [21] is a typical nonlinear technique, which can estimate the CR and QCR at two different time positions, and its computational complexity is much lower than these linear algorithms. However, its signal-to-noise ratio (SNR) threshold is high because it only complete energy accumulation in the lag time domain. To improve the anti-noise performance, the local polynomial Winger distribution (LPWD) [22], the Keystone time-Chirp rate distribution (KTCRD) [23], the scaled Fourier transform (SFT)-based method [24], the chirp rate-quadratic chirp rate distribution (CRQCRD) [25], the modified Lv's distribution (MLVD) [26], the modified CRQCRD (MCRQCRD) [27], the generalized decoupling technique (GDT) [28] and the coherently integrated generalized CPF (CIGCPF) [29], have been presented.

These above-mentioned nonlinear algorithms usually employ fourth order autocorrelation functions (FOAFs) to reduce phase order, and then realize energy accumulation via certain operations. Compared with the CPF, their anti-noise performance and cross-term suppression are certainly enhanced. Nevertheless, due to the fourth order nonlinearity, their anti-noise performance and cross-term suppression are still dissatisfactory.

On the basis of the consideration that a lower order AF method may improve anti-noise performance and cross-term suppression further, we proposed a parameter estimation method named the coherently integrated trilinear autocorrelation function (CITAF) [30], in which a constant delay is needed. Unlike the CITAF, in this paper, a new parameter estimation method based on the third order AF (TOAF) without constant delay is proposed, and the corresponding ISAR imaging algorithm is also given. In the proposed method, a novel TOAF is designed first. Then, by employing the integral operation and multiplication operations, the signal energy is accumulated into a inclined line on a two dimensional (2-D) plane. In realistic application, because the receive data is discrete, the integral operation can be implemented via the nonuniform fast FT (NUFFT) operation, which can reduce the computational complexity. Finally, we complete energy accumulation along the inclined line via Hough transform, and a peak can be obtained in the CR-QCR distribution. According to the peak's coordinates, the parameter estimates which are utilized to compensate the time varying Doppler frequency spread can be obtained. Theoretical analysis and simulation results show that the proposed method has better parameter estimation performance in comparison with several state-of-the-art methods.

The layout of this paper is as follows. In Section II, the ISAR imaging model of the nonuniformly rotating target is given, and the principle of TOAF-based parameter estimation method is introduced in detail. The cross-term suppression, anti-noise performance, estimation accuracy, and computational complexity of the TOAF-based method are analyzed in Section III. Based on the TOAF, the ISAR imaging algorithm and simulation results are provided in Section IV. Section V concludes this paper.

II. ISAR IMAGING MODEL AND PRINCIPLE OF TOAF-BASED PARAMETER ESTIMATION METHOD

A. ISAR IMAGING MODEL

For ISAR imaging of nonuniformly rotating targets with severe maneuverability, the geometry used here is based on the model in [25]. According to [25], after the range migration compensation and translation-induced phase error correction, azimuth echoes of the lth range cell can be modeled as multicomponent CPSs,

$$\begin{aligned} & x_l(t_n) \\ & = s_l(t_n) + z(t_n) \\ & = \sum_{p=1}^{P} A_p \exp\left[j2\pi\left(\alpha_p t_n + \beta_p t_n^2/2 + \gamma_p t_n^3/6\right)\right] + z(t_n), \end{aligned} \tag{1}$$

where t_n denotes the slow time and its sampling frequency is same as the pulse repletion frequency (PRF). P is the number of scatterers in the lth range cell. A_p, α_p, β_p and γ_p denote the amplitude, centroid frequency (CF), CR, and QCR of the pth scatterer, respectively. $z(t_n)$ stands for the additive complex white Gaussian noise.

For ISAR imaging with the CPS model, CR and QCR will cause the Doppler frequency spread. In order to reconstruct a well-focused ISAR image, an effective parameter estimation algorithm is required to compensate the Doppler frequency spread [23]–[29]. In the following subsection, we will introduce a TOAF-based method to solve this problem.

B. PRINCIPLE OF TOAF-BASED PARAMETER ESTIMATION METHOD

We first define a second order AF

$$\mathrm{SOAF}(t_n, \tau_n) = x(t_n + \tau_n)\, x(t_n - \tau_n), \tag{2}$$

where τ_n denotes the lag-time variable. Substituting (1) into (2) yields

$$\begin{aligned} & \mathrm{SOAF}(t_n, \tau_n) \\ & = \underbrace{\sum_{p=1}^{P} A_p^2 \exp\left[j2\pi\left(2\alpha_p t_n + \beta_p t_n^2 + \gamma_p t_n^3/3\right)\right]}_{\text{auto-terms}} \\ & \quad \underbrace{\times \exp\left[j2\pi\left(\beta_p + \gamma_p t_n\right)\tau_n^2\right]}_{\text{auto-terms}} \\ & \quad \underbrace{+\mathrm{SOAF}_{\text{c-terms}}(t_n, \tau_n)}_{\text{cross-terms}} + \underbrace{\mathrm{SOAF}_{\text{n-terms}}(t_n, \tau_n)}_{\text{noise-terms}}, \end{aligned} \tag{3}$$

where $\mathrm{SOAF}_{\text{c-terms}}(t_n, \tau_n)$ and $\mathrm{SOAF}_{\text{n-terms}}(t_n, \tau_n)$ are the cross-terms and noise terms, respectively. Note that (3) can be rearranged as

$$\begin{aligned}&\mathrm{SOAF}(t_n, \tau_n)\\&= \sum_{p=1}^{P} A_p^2 s_p(2t_n) \exp\left[j2\pi\left(\beta_p + \gamma_p t_n\right)\left(\tau_n^2 - t_n^2\right)\right]\\&\quad + \mathrm{SOAF}_{\text{c-terms}}(t_n, \tau_n) + \mathrm{SOAF}_{\text{n-terms}}(t_n, \tau_n).\end{aligned} \tag{4}$$

To compensate $s_p(2t_n)$, a novel TOAF is defined as

$$\mathrm{TOAF}(t_n, \tau_n) = x(t_n + \tau_n)\, x(t_n - \tau_n)\, x^*(2t_n), \tag{5}$$

where '$*$' denotes the complex conjugate. Substituting (1) into (5), we can obtain

$$\begin{aligned}&\mathrm{TOAF}(t_n, \tau_n)\\&= \underbrace{\sum_{p=1}^{P} A_p^3 \exp\left[-j2\pi\left(\beta_p + \gamma_p t_n\right) t_n^2\right] \exp\left[j2\pi\left(\beta_p + \gamma_p t_n\right)\tau_n^2\right]}_{\text{auto-terms}}\\&\quad \underbrace{+\mathrm{TOAF}_{\text{c-terms}}(t_n, \tau_n)}_{\text{cross-terms}} + \underbrace{\mathrm{TOAF}_{\text{n-terms}}(t_n, \tau_n)}_{\text{noise-terms}},\end{aligned} \tag{6}$$

where $\mathrm{TOAF}_{\text{c-terms}}(t_n, \tau_n)$ and $\mathrm{TOAF}_{\text{n-terms}}(t_n, \tau_n)$ are the cross-terms and noise terms, respectively. Then, we accumulate the signal energy along the lag-time axis by the integral operation

$$\begin{aligned}&R_0\left(t_n, F_{\tau_n}\right)\\&= \int_{\tau_n} \mathrm{TOAF}(t_n, \tau_n) \exp\left(-j2\pi F_{\tau_n}\tau_n^2\right) d\tau_n\\&= \sum_{p=1}^{P} A_p^3 \exp\left[-j2\pi\left(\beta_p + \gamma_p t_n\right) t_n^2\right]\\&\quad \times \int_{\tau_n} \exp\left\{-j2\pi\left[F_{\tau_n} - \left(\beta_p + \gamma_p t_n\right)\right]\tau_n^2\right\} d\tau_n\\&\quad + \int_{\tau_n} \mathrm{TOAF}_{\text{c-terms}}(t_n, \tau_n) \exp\left(-j2\pi F_{\tau_n}\tau_n^2\right) d\tau_n\\&\quad + \int_{\tau_n} \mathrm{TOAF}_{\text{n-terms}}(t_n, \tau_n) \exp\left(-j2\pi F_{\tau_n}\tau_n^2\right) d\tau_n\\&= \underbrace{\sum_{p=1}^{P} A_p' \exp\left[-j2\pi\left(\beta_p + \gamma_p t_n\right) t_n^2\right] \delta\left[F_{\tau_n} - \left(\beta_p + \gamma_p t_n\right)\right]}_{\text{auto-terms}}\\&\quad + \underbrace{R_{0,\text{c-terms}}\left(t_n, F_{\tau_n}\right)}_{\text{cross-terms}} + \underbrace{R_{0,\text{n-terms}}\left(t_n, F_{\tau_n}\right)}_{\text{noise-terms}},\end{aligned} \tag{7}$$

where F_{τ_n} is the frequency domain corresponding to τ_n, A_p' $R_{0,\text{c-terms}}\left(t_n, F_{\tau_n}\right)$ and $R_{0,\text{n-terms}}\left(t_n, F_{\tau_n}\right)$ are the amplitude, cross-terms and noise terms, respectively. Now, it can be seen, the signal energy has been accumulated into a inclined line in the $t_n - F_{\tau_n}$ distribution. If we want to accomplish the energy accumulation coherently along this straight, the time varying phase term in (7) should be compensated completely.

As we all know, the Dirac delta function satisfies

$$h(f)\,\delta(f - f_0) = h(f_0)\,\delta(f - f_0). \tag{8}$$

Utilizing the above property, (7) can be approximated as

$$\begin{aligned}R_0\left(t_n, F_{\tau_n}\right) = &\sum_{p=1}^{P} A_p' \exp\left(-j2\pi F_{\tau_n} t_n^2\right) \delta\left[F_{\tau_n} - \left(\beta_p + \gamma_p t_n\right)\right]\\&+ R_{0,\text{c-terms}}\left(t_n, F_{\tau_n}\right) + R_{0,\text{n-terms}}\left(t_n, F_{\tau_n}\right).\end{aligned} \tag{9}$$

Then, the time varying phase term, i.e., $\exp\left(-j2\pi F_{\tau_n} t_n^2\right)$ can be easily compensated as follows

$$\begin{aligned}&R_1\left(t_n, F_{\tau_n}\right)\\&= R_0\left(t_n, F_{\tau_n}\right) \exp\left(j2\pi F_{\tau_n} t_n^2\right)\\&= \underbrace{\sum_{p=1}^{P} A_p' \delta\left[F_{\tau_n} - \left(\beta_p + \gamma_p t_n\right)\right]}_{\text{auto-terms}}\\&\quad + \underbrace{R_{1,\text{c-terms}}\left(t_n, F_{\tau_n}\right)}_{\text{cross-terms}} + \underbrace{R_{1,\text{n-terms}}\left(t_n, F_{\tau_n}\right)}_{\text{noise-terms}},\end{aligned} \tag{10}$$

where $R_{1,\text{c-terms}}\left(t_n, F_{\tau_n}\right)$ and $R_{1,\text{n-terms}}\left(t_n, F_{\tau_n}\right)$ are the cross-terms and noise terms, respectively. Then, the energy accumulation along the inclined line $F_{\tau_n} = \beta_p + \gamma_p t_n$ is accomplished through the Hough transform [31], [32]. In order to reduce the energy loss in Hough transform, the interpolation technique with a factor 4 is adopted for F_{τ_n}. According to the principle of Hough transform, the coherent integration along the inclined line can be expressed as

$$\begin{aligned}&R(\beta_s, \gamma_s)\\&= \sum_{t_n} R_1\left[t_n, \beta_s + round\left(\gamma_s t_n / \Delta F_{\tau_n}\right)\Delta F_{\tau_n}\right]\\&= \underbrace{\sum_{p=1}^{P} A_p'' \delta\left(\beta_s - \beta_p\right)\delta\left(\gamma_s - \gamma_p\right)}_{\text{auto-terms}}\\&\quad + \underbrace{R_{\text{c-terms}}(\beta_s, \gamma_s)}_{\text{cross-terms}} + \underbrace{R_{\text{n-terms}}(\beta_s, \gamma_s)}_{\text{noise-terms}},\end{aligned} \tag{11}$$

where $round(\cdot)$ denotes the operation that rounds to nearest integer, ΔF_{τ_n} is the frequency interval of F_{τ_n}, A_p'', $R_{\text{c-terms}}(\beta_s, \gamma_s)$ and $R_{\text{n-terms}}(\beta_s, \gamma_s)$ are the amplitude, cross-terms and noise terms, respectively. β_s and γ_s represent the searching CR and QCR, respectively. We set the interval of β_s as integral multiples of ΔF_{τ_n}. $round\left(\gamma_s t_n / \Delta F_{\tau_n}\right)\Delta F_{\tau_n}$ in (11) can be pre-calculated and stored, therefore, (11) can be accomplished though the addition operation.

Obviously, only when the CR and QCR are matched by the searching parameters, the signal along $F_{\tau_n} = (\beta_p + \gamma_p t_n)$ can be accumulated completely. Each scatterer generates a self-term, which accumulates into a sole peak at (β_p, γ_p) in $R(\beta_s, \gamma_s)$. Because the cross-terms cannot be accumulated as the self-terms (this will be analyzed and verified in

Section III.A), β_p and γ_p can be estimated by searching the peak of $|R(\beta_s, \gamma_s)|^2$ as

$$\left(\hat{\beta}_p = \beta_s, \hat{\gamma}_p = \gamma_s\right) = \arg\max_{(\beta_s,\gamma_s)} |R(\beta_s, \gamma_s)|^2, \quad (12)$$

where 'arg max' represents the argument which maximizes. $\hat{\beta}_p$ and $\hat{\gamma}_p$ denote the estimates of the CR and QCR, respectively.

After dechirping $s_l(t_n)$ with $\exp(-j2\pi\hat{\beta}_p t_n^2/2 - j2\pi\hat{\gamma}_p t_n^3/6)$, the estimates of the amplitude and CFwhich are denoted as $\hat{A}_p$ and $\hat{\alpha}_p$, can be obtained via the Fourier transform (FT) operation.

Remark 1: $x(2t_n)$ in (5) requires redundancy information as along as the effective signal length. For example, if the effective signal length is set as 2s, the total signal length should be 4s.

III. PERFORMANCE ANALYSIS AND COMPARISON

In this section, the cross-term suppression, anti-noise performance, estimation accuracy and computational complexity of the proposed method are analyzed. Moreover, several state-of-the-art parameter estimation methods are used to compare with this method.

A. CORSS-TERM SUPPRESSION

According to the definition of TOAF, we know the cross-terms appear. Here, in order to analyze the cross-term suppression performance of the TOAF-based method for simplicity, we consider two noise-free CPSs, i.e., $s_1(t_n)$ and $s_2(t_n)$. A_1, A_2, α_1, α_2, β_1, β_2, γ_1, and γ_2 are the amplitudes, CFs, CRs, and QCRs of these two CPSs, respectively. With these notations, the cross-term can be expressed as

$$\begin{aligned}
&\mathrm{TOAF}_{\text{c-terms}}(t_n, \tau_n) \\
&= s_1(t_n+\tau_n)\, s_1(t_n-\tau_n)\, s_2^*(2t_n) \\
&\quad + s_1(t_n+\tau_n)\, s_2(t_n-\tau_n)\, s_1^*(2t_n) \\
&\quad + s_1(t_n+\tau_n)\, s_2(t_n-\tau_n)\, s_2^*(2t_n) \\
&\quad + s_2(t_n+\tau_n)\, s_1(t_n-\tau_n)\, s_1^*(2t_n) \\
&\quad + s_2(t_n+\tau_n)\, s_1(t_n-\tau_n)\, s_2^*(2t_n) \\
&\quad + s_2(t_n+\tau_n)\, s_2(t_n-\tau_n)\, s_1^*(2t_n). \quad (13)
\end{aligned}$$

The first term of (13) has the form of

$$\begin{aligned}
\mathrm{TOAF}_{\text{c-terms},1}(t_n, \tau_n) &= s_1(t_n+\tau_n)\, s_1(t_n-\tau_n)\, s_2^*(2t_n) \\
&= A_1 \exp\left[j2\pi(\beta_1+\gamma_1 t_n)\tau_n^2\right] \\
&\quad \times \exp\left[-j2\pi(\beta_1+\gamma_1 t_n)t_n^2\right] \\
&\quad \times s_1(2t_n)\, s_2^*(2t_n). \quad (14)
\end{aligned}$$

Performing the integral operation along the lag-time axis as follows

$$\begin{aligned}
&R_{0,c,1}(t_n, F_{\tau_n}) \\
&= \int_{\tau_n} \mathrm{TOAF}_{\text{c-terms},1}(t_n, \tau_n) \exp\left(-j2\pi F_{\tau_n}\tau_n^2\right) d\tau_n \\
&= A_1' \exp\left[-j2\pi(\beta_1+\gamma_1 t_n)t_n^2\right] \\
&\quad \times \delta\left[F_{\tau_n} - (\beta_1+\gamma_1 t_n)\right] s_1(2t_n)\, s_2^*(2t_n), \quad (15)
\end{aligned}$$

where A_1' denotes the amplitude after the integral operation. It can be seen only when $\alpha_1 = \alpha_2$, $\beta_1 = \beta_2$, and $\gamma_1 = \gamma_2$, this term can be accumulated into a peak via the latter operations. However, the accumulated peak locates at the same position as the auto-terms.

The second term of (13) can be expressed as

$$\begin{aligned}
&\mathrm{TOAF}_{\text{c-terms},2}(t_n, \tau_n) \\
&= s_1(t_n+\tau_n)\, s_2(t_n-\tau_n)\, s_1^*(2t_n) \\
&= A_1^2 A_2 \exp\left[j2\pi(\alpha_1-\alpha_2)(t_n+\tau_n)\right] \\
&\quad \times \exp\left[j2\pi(\beta_1-\beta_2)(t_n/2+\tau_n)t_n\right] \\
&\quad \times \exp\left[j\pi(\gamma_1-\gamma_2)\left(t_n^3+3\tau_n t_n^2+\tau_n^3\right)/3\right] \\
&\quad \times \exp\left\{j\pi\left[(\beta_1+\beta_2)+(\gamma_1+\gamma_2)t_n\right]\tau_n^2\right\}. \quad (16)
\end{aligned}$$

Obviously, only when $\alpha_1 = \alpha_2$, $\beta_1 = \beta_2$, and $\gamma_1 = \gamma_2$, (16) can be accumulated into a inclined line by the integral operation along the lag-time axis, and then a peak locates at the same point as the auto-term can be accumulated.

In (13), the sixth term has the same form as the first term, the third, fourth, and fifth terms have the same form as the second term. Thus, we can conclude that the cross-terms do not influence the auto-terms detection.

Remark 2: The cross-terms of the TOAF-based method contain 6 items under two-component CPSs. While for these algorithms which have FOAFs, such as in [22]–[29], the number of cross-terms is 14. Thus the TOAF-based method may have a better cross-term suppression performance than these algorithms.

To illustrate the cross-term suppression performance of the TOAF-based method, an example is given below.

Example 1: Three noise-free CPSs denoted by $S1$, $S2$, and $S3$ are considered. The sampling frequency and effective signal length are 128 Hz and 2s, respectively (2s redundancy information is used). Table 1 gives the signal parameters, and the simulation results are shown in Figure 1.

After the operation of (5), the signal energy distribution on the slow time-lag time plane is shown as in Figure 1(a). Due to the definition of (5) and utilization of redundancy

TABLE 1. Signal parameters.

	Amplitude	CF (Hz)	CR (Hz/s)	QCR (Hz/s^2)
S1	1.0	10	15	30
S2	0.9	10	-20	30
S3	0.8	10	15	-40

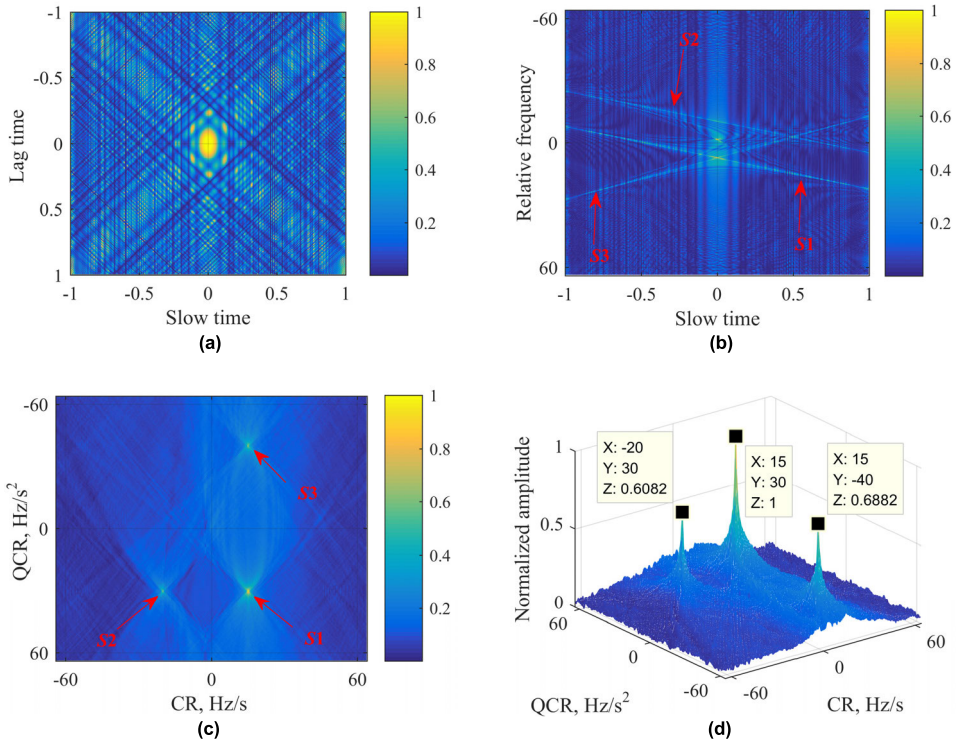

FIGURE 1. Simulation results of Example 1. (a) The normalized slow time-lag time distribution after performing (5). (b) The normalized slow time-relative frequency distribution after performing (7). (c) The normalized imagesc of the CR and QCR distribution. (d) The normalized stereogram of the CR and QCR distribution.

information, the shape of this distribution is a square, not a rhombus any more, which would be benefit the output SNR.

Performing the integral operation along lag time axis, we obtain the slow time-relative frequency distribution as shown in Figure 1(b). It can be seen three auto-terms have been accumulated into three inclined lines. Because of the same QCR, S1 is parallel to S2. Moreover, S1 and S3 are intersect at (0, 15 Hz/s) due to the same CR. Then, after phase compensation and coherent accumulation, we obtain the CR-QCR distribution as shown in Figure 1(c). It is seen from the corresponding stereogram in Figure 1(d), three well focused peaks appear and can be easily detected, while the cross-terms are not been accumulated. Based on the peaks' coordinates on the plane, the CRs and QCRs of these three–component CPSs can be precisely estimated.

B. ANTI-NOISE PERFORMANCE

In this subsection, the input-output SNR is used to evaluate the anti-noise performance [29], [30], and the output SNR of the TOAF-based method is deduced in closed form.

We start with a noisy CPS in the discrete form as

$$\begin{aligned} x(n) &= s(n) + z(n) \\ &= A_0 \exp\left[j2\pi\left(\alpha_0 n T_s + \beta_0 (nT_s)^2/2 + \gamma_p (nT_s)^3/6\right)\right] \\ &\quad + z(n), (n = -N/2, -N/2+1, \cdots, N/2-1), \end{aligned} \tag{17}$$

where A_0 is the amplitude, T_s is the sampling interval, N is the number of effective samples, and $z(n)$ is a zero-mean white Gaussian noise with the variance of σ^2. The input SNR is defined as $\mathrm{SNR}_{\mathrm{in}} = A_0^2/\sigma^2$. The output SNR of the proposed method is defined as [29], [30],

$$\begin{aligned} &\mathrm{SNR}_{\mathrm{out}}^{\mathrm{TOAF}} \\ &= \frac{|R_s(\beta_0, \gamma_0)|^2}{var\left[R_{zs}(\beta_0, \gamma_0)\right]} \\ &= \frac{|R_s(\beta_0, \gamma_0)|^2}{E\left[R_{zs}(\beta_0, \gamma_0) R_{zs}^*(\beta_0, \gamma_0)\right] - |E\left[R_{zs}(\beta_0, \gamma_0)\right]|^2}, \end{aligned} \tag{18}$$

where $R_s(\beta_0, \gamma_0)$ and $R_{zs}(\beta_0, \gamma_0)$ denote the results of the TOAF-based method at (β_0, γ_0) in the absence and presence of noise, respectively, var$[\cdot]$ and $E[\cdot]$ denote the variance and expected value of its argument, respectively.

Let

$$\begin{cases} e^{j\varphi(\beta,\gamma,m,n)} = \exp\left[-j2\pi\left(\beta + \gamma n T_s\right)\left(m^2 T_s^2 - n^2 T_s^2\right)\right], \\ s_1 = s(n+m), s_2 = s(n-m), s_3 = s(2n), \\ z_1 = z(n+m), z_2 = z(n-m), z_3 = z(2n), \end{cases} \tag{19}$$

where $m = -N/2, -N/2+1, \cdots, N/2-1$. With these expressions, we have

$$R_s(\beta_0, \gamma_0) = \sum_n \sum_m s_1 s_2 s_3^* e^{j\varphi(\beta,\gamma,m,n)} = N^2 A_0^3, \tag{20}$$

$$R_{zs}(\beta_0, \gamma_0) = \sum_n \sum_m (s_1+z_1)(s_2+z_2)(s_3+z_3)^* e^{j\varphi(\beta,\gamma,m,n)}, \tag{21}$$

and

$$\begin{aligned} &E[R_{zs}(\beta_0, \gamma_0)] \\ &= \sum_n \sum_m \left[s_1 s_2 s_3^* + s_1 E\left(z_2 z_3^*\right) + s_2 E\left(z_1 z_3^*\right)\right] e^{j\varphi(\beta,\gamma,m,n)} \\ &= \sum_n \sum_m \left[A_0^3 + A_0\sigma^2\delta(n+m) + A\sigma^2\delta(-n+m)\right] \\ &= N^2 A_0^3 + 2NA_0\sigma^2. \end{aligned} \tag{22}$$

$E\left[R_{zs}(\beta_0, \gamma_0) R_{zs}^*(\beta_0, \gamma_0)\right]$ is calculated in Appendix. Substituting (20), (22) and (33) into (18) gets

$$\mathrm{SNR}_{\mathrm{out}}^{\mathrm{TOAF}} = \frac{3N^2\mathrm{SNR}_{\mathrm{in}}^3}{11N\mathrm{SNR}_{\mathrm{in}}^2 + 42\mathrm{SNR}_{\mathrm{in}} + 18}. \tag{23}$$

Then, we use an example to verify the theoretical output SNR of the TOAF-based method.

Example 2: For convenience, mono-CPS is considered, and its CF, CR, and QCR are: 18 Hz, 5 Hz/s, and 10 Hz/s^2, respectively. The sampling frequency and effective signal length are 128 Hz and 2s, complex white Gaussian noise is added to the signal. The input SNR and output SNR have been converted into deciblels (dBs). The input SNRs are [-12:1:2] dB, 2000 trials are performed for each input SNR value. Several representative algorithms are used to compare with the proposed method, and the simulation results are given in Figure 2.

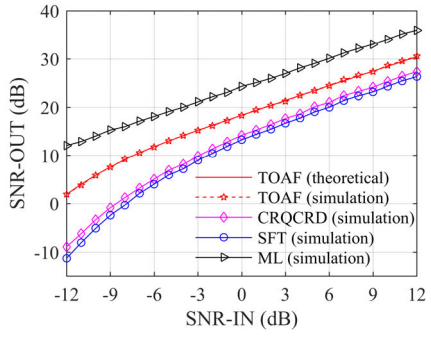

FIGURE 2. Comparisons of the output SNRs.

It can be seen the practical result of the TOAF-based method has a good agreement with the theoretical deduction. The ML method has the best input-output SNR performance due to its linear implementation. Compared with the ML method, because of the nonlinear AFs, the SFT-based method, the CRQCRD and the TOAF-based method have some SNR losses. At high input SNR, the output SNR of the CRQCRD outperforms the SFT-based method about 1 dB due to the introduction of a constant delay, and the TOAF-based method has 3 dB improvement in comparison with the CRQCRD because the following reasons:

1) The AF of the proposed method is third order, while the CRQCRD is fourth order;

2) Both of the proposed method and the CRQCRD use redundancy information, if the effective signal length is N, the total signal length should be $2N$. Because of the introduction of a constant delay in the CRQCRD, the signal distribution after performing the FOAF is shown as in Figure 3. In the propose method, there is no constant delay, therefore, after performing the TOAF, the obtained signal is distributed as a square as shown in Figure 1(a). It can be seen the number of data samples in Figure 1(a) is more than those of Figure 3. This would be helpful to improve the output SNR further, since the energy integration is completed coherently along the slow time and lag time.

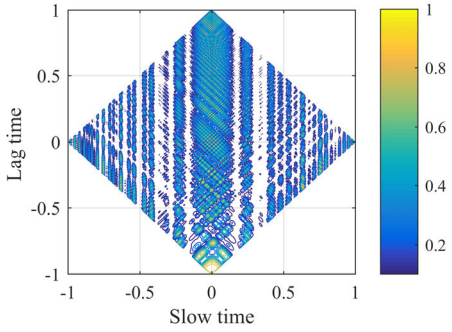

FIGURE 3. The normalized slow time-lag time distribution after performing the FOAF in CRQCRD.

Then, we define another kind of output SNR [25] as

$$\mathrm{SNR}_{\mathrm{out}} = \frac{1}{N\sigma^2}\left|\sum_{n=-N/2}^{N/2} s_p(n)\exp\left[-j2\pi\left(\hat{\alpha}_p n T_s + \hat{\beta}_p n^2 T_s^2/2 + \hat{\gamma}_p n^3 T_s^3/6\right)\right]\right|^2, \tag{24}$$

where N is the effective signal length, and T_s denotes the sampling interval. After compensating $s_p(t_n)$ with $\hat{a}_p$, $\hat{\beta}_p$, and $\hat{\gamma}_p$, the output SNR defined in (24) equals to the energy ratio between the signal and noise. We use (24) to measure the SNR thresholds of the proposed method and some other representative methods. The SNR threshold means a certain value that is to say, when the input SNR is higher than this value, precise estimates can be obtained. 500 trials are performed for each input SNR value, and the simulation results which have been converted into dBs are shown in Figure 4. The ideal output SNR is also given, which is obtained under the assumption that the parameters are exactly estimated at any input SNRs, i.e., the estimated parameters in (24) are equal to the corresponding signal parameters.

It can be seen the SNR threshold of LPWD is -2 dB, which is because a FOAF is used and the energy accumulation is accomplished only in one dimension.

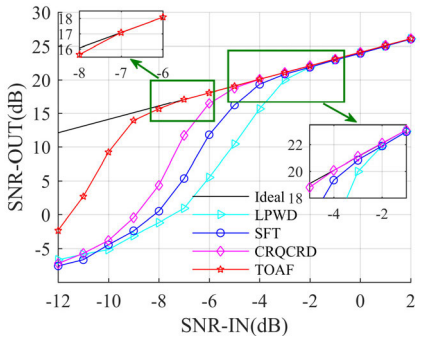

FIGURE 4. Input-output SNR performance.

Although the SFT-based method also uses FOAF, the signal energy is accumulated in 2-D coherently, and its SNR threshold can reach to -3 dB. On the basis of SFT-based method, the CRQCRD utilizes a constant delay in the FOAF. Thus, the output SNR performance of CRQCRD outperforms the SFT-based method and its SNR threshold is -4 dB.

Due to the definition of TOAF, 2-D energy integration, and utilization of redundancy information, it is obvious that the SNR threshold is -7 dB, which has 3 dB improvement in comparison with the CRQCRD.

The comparison result in Figure 4 conforms to the results in Figure 2. Because the input-output SNR performance can reflect the anti-noise performance, we have the conclusion that the proposed method has better anti-noise performance than the other three methods.

Now, we use an example to evaluate the anti-noise performance of the TOAF-based method under noisy multicomponent CPSs. The CRQCRD and SFT-based method are used for comparison.

Example 3: The signal parameters are the same as those of Example 1. Complex white Gaussian noise is added to the signals, and the input SNRs are -7 dB for $S1$, -4 dB for $S2$ and -3 dB for $S3$. Simulation results are given in Figure 5.

Obviously, in Figure 5(a), due to the poor input-output performance, only the peak corresponding to $S3$ is identifiable through the SFT-based method. $S1$ and $S2$ are submerged by the noise and cross-terms. The input SNR of $S1$ is lower than the SNR threshold of CRQCRD, thus, $S1$ is submerged, $S2$ and $S3$ are identifiable in Figure 5(b). With the TOAF-based method, three peaks all appear and exactly locate at the points corresponding to these three component CPSs in Figure 5(c).

The above simulation results further verify the proposed method has better anti-noise performance even under noisy multicomponent CPSs.

C. ESTIMATION ACCURACY

In this subsection, the mean square errors (MSEs) of the estimated CR and QCR are applied to characterize the estimation accuracy [25]–[28].

Example 4: The simulation conditions are the same as those of Example 2. 500 trials are performed for each input SNR value. The TOAF-based method and CRQCRD are both use 2s redundancy information, whereas no redundancy information is used by the SFT-based method and LPWD. Thus the Cramer-Rao lower bounds (CRLBs) [33] corresponding to N and $2N$ samples are both presented. Simulation results are shown in Figure 6.

It can be seen, when the input SNR is higher than a certain threshold, the MSEs of CR and QCR are close to the CLRBs. The SNR thresholds for TOAF-based method, CRQCRD, SFT-based method and LPWD are -7 dB, -4 dB, -3 dB, and -2 dB, respectively. These results are conformed to SNR thresholds obtained in Figure 4. This can also illustrate the anti-noise performance of these four methods.

Moreover, due to the utilization of redundancy information, the MSEs of the estimated CRs and QCRs via the TOAF-based method and CRQCRD are lower than those of the SFT-based method and LPWD.

D. COMPUTATIONAL COMPLEXITY

I this subsection, we compare the computational complexities of the TOAF-based method, CRQCRD, SFT-based method, and LWPD in terms of the number of complex multiplications. Denote the effective length of the signal by N.

For the TOAF-based method, there are four steps. First, the calculation of the TOAF in (5) is $[O(2N^2)]$. Second, utilize the NUFFT operation to accomplish the integral operation in (7). Because the interpolation technique with a factor 4 for F_{τ_n} is adopted in the implementation of this method, the length of NUFFT should be $4N$, and the calculation of (7) is $[O(8N^2\log_2 N+16N^2)]$. Third, compensate the time varying phase term $[O(4N^2)]$. Finally, complete the coherent accumulation along $F_{\tau_n} = \beta_p + \gamma_p t_n$, which can be efficiently implemented by complex addition operations. Thus, the total number of complex multiplications of the TOAF-based method is in the order of $[O(8N^2\log_2 N + 22N^2)]$.

The main implementation procedures of the CRQCRD include the calculation of FOAF $[O(1.5N^2)]$, chirp-z-based SFT operation $[O(3N^2\log_2 N)]$ [34], and NUFFT operation $[O(2N^2\log_2 N)]$ [35]. Thus, the total computational complexity of the CRQCRD is in the order of $[O(5N^2\log_2 N + 1.5N^2)]$.

For the SFT-based method, the implementation procedure is as the same as the CRQCRD, therefore the total computational complexity is also in the order of $[O(5N^2\log_2 N + 1.5N^2)]$.

The main steps of LPWD include the calculation of FOAF $[O(1.5N^2)]$, and the 2-D parameter searching procedure to acquire maximum value $[O(N^3)]$. As a result, the total computational complexity is about $[O(N^3 + 1.5N^2)]$.

The computational complexities and SNR thresholds of these methods are listed in Table 2. Figure 7 shows the computational complexities of these four methods versus the number of effective signal samples. The results show that the TOAF-based method has the lowest SNR threshold, while the computational complexity remains proper. Thus, the TOAF-based method is more applicable for the CPS.

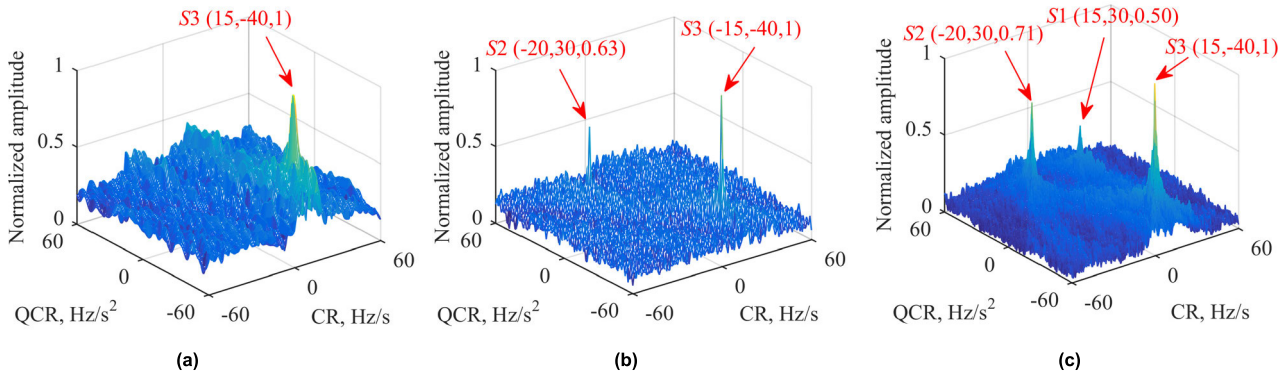

FIGURE 5. Simulation results of Example 3. (a) The result of SFT-based method. (b) The result of CRQCRD. (c) The result of TOAF-based method.

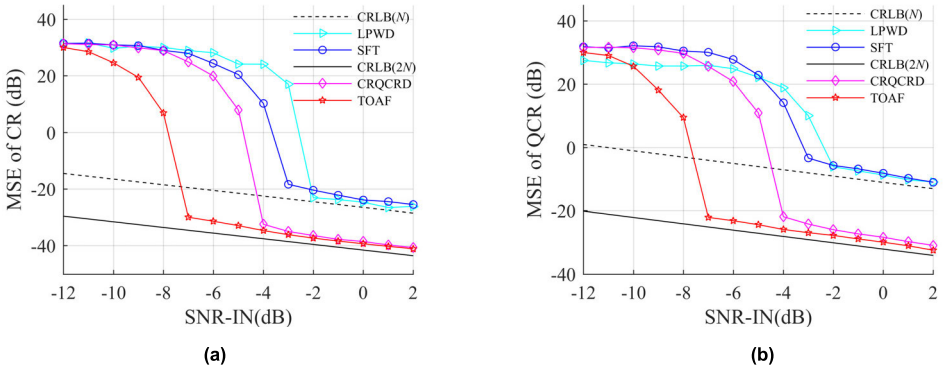

FIGURE 6. Estimation accuracy comparison results. (a) MSEs of CR. (b) MSEs of QCR.

TABLE 2. Comparisons of computational complexity and SNR threshold.

Algorithm	Computational complexity	SNR threshold
TOAF-based method	$O(8N^2\log_2 N+22N^2)$	-7 dB
CRQCRD	$O(5N^2\log_2 N+1.5N^2)$	-4 dB
SFT-based method	$O(5N^2\log_2 N+1.5N^2)$	-3 dB
LPWD	$O(N^3+1.5N^2)$	-2 dB

IV. THE TOAF-BASED ISAR IMAGING ALFORITHM AND COMPARISON

Based on the TOAF, an ISAR imaging algorithm of nonuniformly rotating target is given, and the comparison results with the CRQCRD-based ISAR imaging algorithm, SFT-based ISAR imaging algorithm, and LPWD-based ISAR imaging algorithm are given in this section.

A. ISAR IMAGING ALGORITHM BASED ON THE TOAF

The implementation of the proposed ISAR imaging algorithm is illustrated in detail as follows.

Step 1) After completing the range compression and the translational motion compensation, the radar echoes are corrected into the right range cell.

Step 2) Get the signal data $s_l(t_n)$ (where $1 \le l \le L$ and L is the number of range cells), and set $s_l'(t_n)=0$, the $s_l'(t_n)$ is used to store the reconstructed signals for the scatterers.

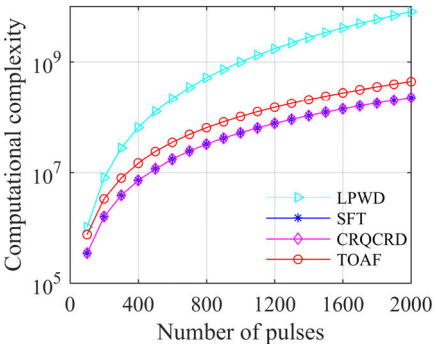

FIGURE 7. Computational complexity versus the number of effective signal samples.

Step 3) Applying the TOAF-based method to $s_l(t_n)$, we can obtain the estimates $\hat{\beta}_p$ and $\hat{\gamma}_p$ of the pth scatterer.

Step 4) Dechirping $s_l(t_n)$ with $\exp(-j2\pi\hat{\beta}_p t_n^2/2 - j2\pi\hat{\gamma}_p t_n^3/6)$, the estimates of A_p and α_p can be obtained as

$$\left(\hat{A}_p=\frac{D'}{N},\hat{\alpha}_p=\hat{F}_{t_n}\right) = \underset{(D,F_{t_n})}{\arg\max}\left|FT\left\{s_l(t_n)\exp\left[j2\pi\left(-\frac{\hat{\beta}_p}{2}t_n^2-\frac{\hat{\gamma}_p}{6}t_n^3\right)\right]\right\}\right|, \tag{25}$$

where D' denotes the peak amplitude after the FT operation, and F_{t_n} is the frequency domain corresponding to t_n.

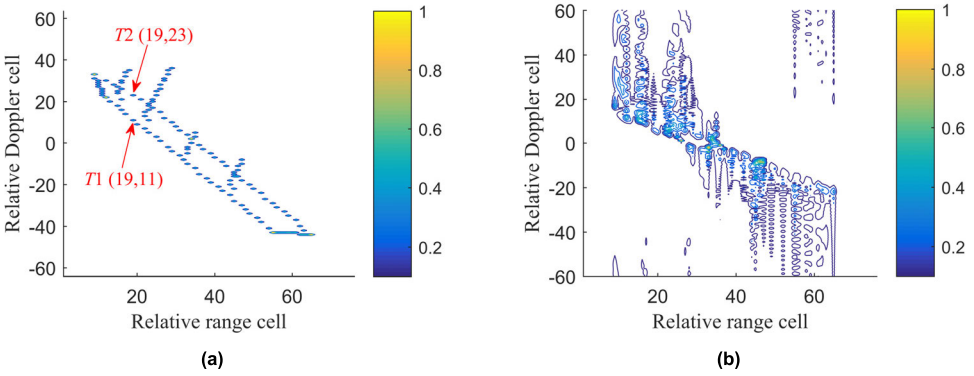

FIGURE 8. (a) Target scatterer model. (b) ISAR image based on the RD algorithm.

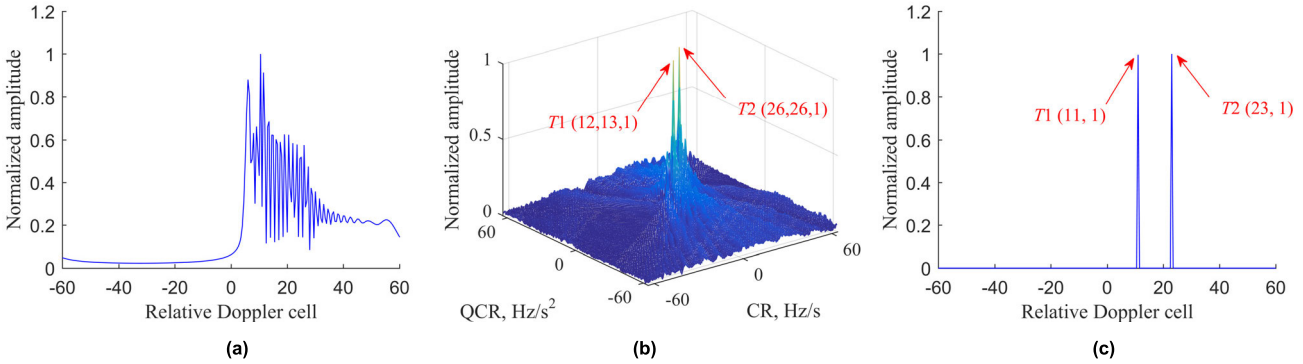

FIGURE 9. Simulation results of performing the RD method and the TOAF-based method in the 19th range cell. (a) Result of the RD method. (b) Result of the TOAF-based method in the CR-QCR distribution. (c) Result of the RD method after compensation with the estimated parameters obtained in (b).

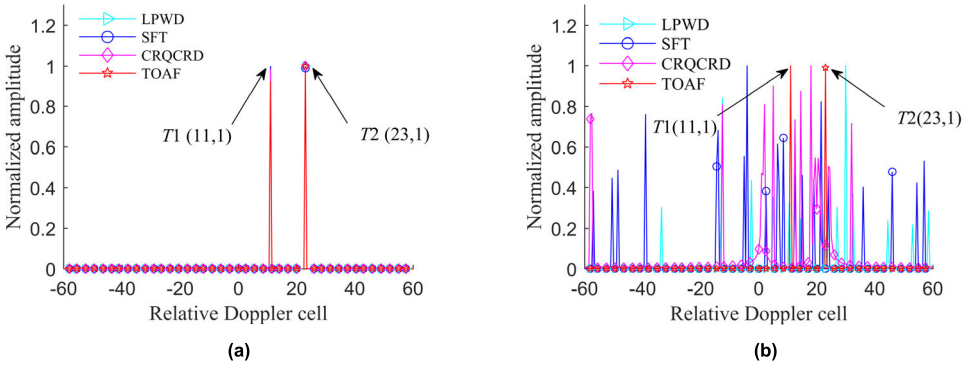

FIGURE 10. Results of compensation simulation. (a) $\mathrm{SNR}_{IN} = -1$ dB. (b) $\mathrm{SNR}_{IN} = -6$ dB.

The FT operation can be implemented via the FFT operation in realistic application.

Step 5) Set $s_l'(t_n) = s_l'(t_n) + \hat{A}_p \exp\left(j2\pi \hat{a}_p t_n\right)$.

STEP 6) Subtract the estimated pth CPS from $s_l(t_n)$

$$s_l(t_n) = s_l(t_n) - \hat{A}_p \exp\left[j2\pi\left(\hat{\alpha}_p t_n + \frac{\hat{\beta}_p}{2}t_n^2 + \frac{\hat{\gamma}_p}{6}t_n^3\right)\right]. \tag{26}$$

Step 7) Repeat steps 3) −6) until the residual signal energy $l < L$ is less than $l < L$, which is an energy threshold.

Step 8) If $l < L$, set $l = l + 1$ and repeat steps 3) −7) until $l = L$.

Now, the Doppler frequency spread in all range cells has been compensated with the estimated parameters, and the signals of the scatterers have been reconstructed. Performing the RD technique on $s_l'(t_n)$ $(1 \le l \le L)$, the well-focused RD image for nonuniformly rotating targets can be obtained.

The above-mentioned is the proposed ISAR imaging algorithm. In the next subsection, we will use some numerical examples to validate the proposed ISAR imaging algorithm.

B. NUMERICAL EXAMPLES AND COMPARISON

In this subsection, a fluctuating ship shown in Figure 8(a) is modeled as a set of ideal scatterers. ISAR imaging algorithms, which utilize the RD method, LPWD, SFT-based

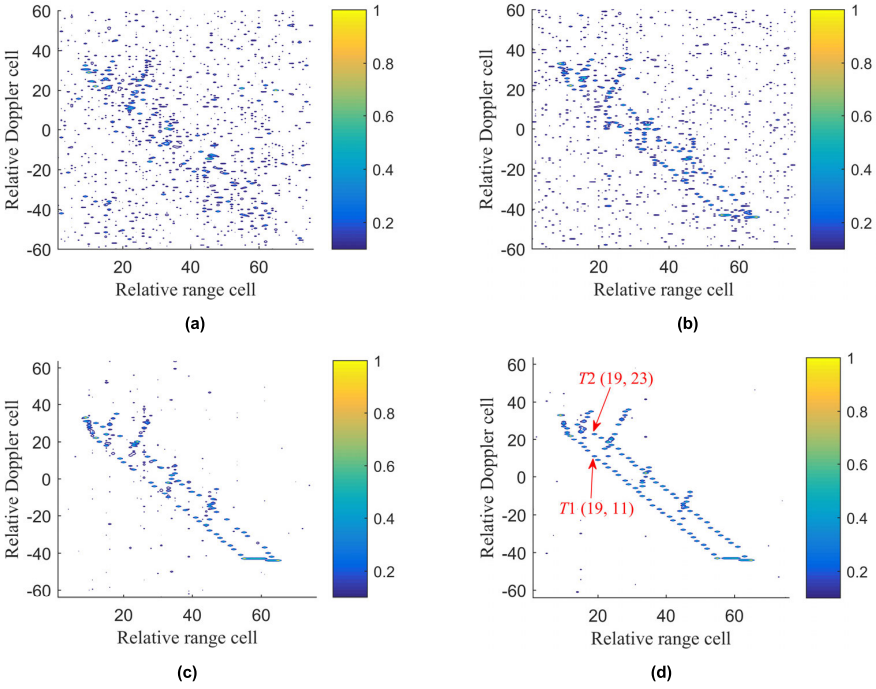

FIGURE 11. ISAR images. (a) ISAR imaging result based on the LPWD. (b) ISAR imaging result based on the SFT. (c) ISAR imaging result based on the CRQCRD. (d) ISAR imaging result based on the proposed method.

TABLE 3. Parameters of radar and target.

Carrier frequency	5 GHz	PRF		128 Hz	
Bandwidth	100 MHz	Effective echo pulses N		256	
Rotating coefficient		X axis	Y axis	Z axis	
Constant term		0.015 rad/s	0.01 rad/s	0.01 rad/s	
First term		0.02 rad/s^2	0.02 rad/s^2	0.01 rad/s^2	
Second term		0.01 rad/s^3	0.02 rad/s^3	0.01 rad/s^3	

method, CRQCRD and TOAF-based method, are adopted on this ship model. The parameters of the radar and moving target are listed in Table 3.

Figure 8(b) is the RD image after the range migration compensation and translation-induced phase error correction. Through the comparison between Figures 8(a) and 8(b), it can be seen because of the Doppler frequency spread induced by the CR and QCR, a well-focused ISAR image can't be obtained by the conventional RD method. Therefore, we need to estimate the CR and QCR to compensate the Doppler frequency spread.

In Figure 8(a), two scatterers $T1$ and $T2$ in the 19th range cell are closely adjacent, and their CRs and QCRs are (12, 13) and (26, 26), respectively. The simulation result of the RD method without the Doppler frequency spread compensation, is given in Figure 9(a). From the figure, these two scatterers can't be recognized.

Applying the TOAF-based method in the 19th range cell, the result as shown in Figure 9(b) is get. Obviously, the TOAF-based method can distinguish these two closely adjacent scatterers easily, and the CRs and QCRs can be estimated correctly. With these estimates obtained in Figure 9(b), after compensating the Doppler frequency spread through applying (25) on the signals of the 19th range cell, $T1$ and $T2$ are visible clearly in Figure 9(c). The results of this simulation illustrate that the TOAF-based method can compensate the Doppler frequency spread effectively.

Now we add the complex white Gaussian noise to the signals, the input SNR is defined as $\mathrm{SNR_{IN}} = 10\log_{10}(P_s/P_n)$ (where P_s and P_n denote the input signal power and the noise power, respectively), and the input SNR is set as -1 dB first. After compensating the Doppler frequency spread via the LWPD, SFT-based method, CRQCRD and TOAF-based method in the 19th range cell, it is obvious in Figure 10(a) that all these four methods are effective.

However, when under a lower SNR environment, i.e., $\mathrm{SNR_{IN}} = -6$ dB, from the results shown in Figure 10(b), it can be seen only the TOAF-based method can recognize $T1$ and $T2$ successfully, while the LPWD, SFT-based method and CRQCRD are invalid. To observe the image quality intuitively, the normalized ISAR imaging results obtained through these four methods under $\mathrm{SNR_{IN}} = -6$ dB are also given in Figure 11. The energy threshold is set as 6% of the original signal energy, which can guarantee that the weak scatterers will not be lost. The entropy [17] is selected as a criterion and the results are listed in Table 4. The better focused image results in a smaller entropy.

Due to the poor anti-noise performance of the LPWD, and SFT-based method, the ship image is fully submerged in the spurious scatterers as shown in Figures 11(a)-(b).

TABLE 4. Entropies of ISAR images in Figure. 11.

	Figure 11(a)	Figure 11(b)	Figure 11(c)	Figure 11(d)
Entropies	126.45	115.35	57.31	42.96

The CRQCRD has better estimation performance than these two method. Thus, the entropy of Figure 11(c) is smaller. For the proposed method, almost all the CPSs can be estimated correctly, the image quality of Figure 11(d) is much better than that of Figures 11(a)-(c), which conforms to the entropies listed in Table 4.

V. CONCLUSION

In this paper, we propose an ISAR imaging algorithm based on the TOAF for non-uniformly rotating targets. The main characteristics of this method include: 1) A novel TOAF is designed; 2) Redundancy information is utilized; 3) 2-D coherent energy accumulation is accomplished; 4) It can be efficiently implemented via the NUFFT, multiplication and addition operations. Owing to these characteristics, the proposed method significantly enhances the anti-noise performance in comparisons with several state-of-the-art algorithms, such as the LPWD, SFT-based method, and CRQCRD, while offering a proper computational complexity. The performance analyses and the results of some numerical examples validate the effectiveness and superiority of the proposed method.

APPENDIX

In this Appendix, $E\left[R_{zs}\left(\beta_0,\gamma_0\right)R_{zs}^{*}\left(\beta_0,\gamma_0\right)\right]$ in (18) is calculated. Let

$$\begin{cases} e^{j\varphi(\beta,\gamma,p,q)}=\exp\left[-j2\pi\left(\beta+\gamma qT_s\right)\left(p^2T_s^2-p^2T_s^2\right)\right], \\ s_4=s\left(q+p\right),\ s_5=s\left(q-p\right),\ s_6=s\left(2q\right), \\ z_4=z\left(q+p\right),\ z_5=z\left(q-p\right),\ z_6=z\left(2q\right), \\ \Phi=e^{j\varphi(\beta,\gamma,m,n)}e^{j\varphi(\beta,\gamma,p,q)}. \end{cases} \tag{27}$$

Then, we have (28), as shown at the bottom of this page.

These four terms of (28) equal to (29), (30), (31), and (32), as shown at the bottom of this page respectively.

$$\begin{aligned} E\left[R_{zs}\left(\beta_0,\gamma_0\right)R_{zs}^{*}\left(\beta_0,\gamma_0\right)\right] &= \sum_n\sum_m\sum_q\sum_p\left[\begin{array}{l}\left(s_1+z_1\right)\left(s_2+z_2\right)\left(s_3+z_3\right)^* \\ \times\left(s_4+z_4\right)^*\left(s_5+z_5\right)^*\left(s_6+z_6\right)\end{array}\right]\Phi \\ &= \sum_n\sum_m\sum_q\sum_p s_1s_2s_3^*s_4^*s_5^*s_6\Phi+\sum_n\sum_m\sum_q\sum_p \\ &\quad\times E\left[\begin{array}{l}s_2s_4^*s_5^*s_6\left(z_1z_3^*\right)+s_2s_3^*s_5^*s_6\left(z_1z_4^*\right)+s_2s_3^*s_4^*s_6\left(z_1z_5^*\right) \\ +s_1s_4^*s_5^*s_6\left(z_2z_3^*\right)+s_1s_3^*s_5^*s_6\left(z_2z_4^*\right)+s_1s_3^*s_4^*s_6\left(z_2z_5^*\right) \\ +s_1s_2s_4^*s_5^*\left(z_3^*z_6\right)+s_1s_2s_3^*s_5^*\left(z_4^*z_6\right)+s_1s_2s_3^*s_4^*\left(z_5^*z_6\right)\end{array}\right]\Phi \\ &\quad+\sum_n\sum_m\sum_q\sum_p \\ &\quad\times E\left[\begin{array}{l}s_1s_3^*\left(z_2z_4^*z_5^*z_6\right)+s_1s_4^*\left(z_2z_3^*z_5^*z_6\right)+s_1s_5^*\left(z_2z_3^*z_4^*z_6\right) \\ +s_2s_3^*\left(z_1z_4^*z_5^*z_6\right)+s_2s_4^*\left(z_1z_3^*z_5^*z_6\right)+s_2s_5^*\left(z_1z_3^*z_4^*z_6\right) \\ +s_3^*s_6\left(z_1z_2z_4^*z_5^*\right)+s_4^*s_6\left(z_1z_2z_3^*z_5^*\right)+s_5^*s_6\left(z_1z_2z_3^*z_4^*\right)\end{array}\right]\Phi \\ &\quad+\sum_n\sum_m\sum_q\sum_p E\left(z_1z_2z_3^*z_4^*z_5^*z_6\right)\Phi \end{aligned} \tag{28}$$

$$\sum_n\sum_m\sum_q\sum_p A_0^6=N^4A_0^6, \tag{29}$$

$$\begin{aligned} &\sum_n\sum_m\sum_q\sum_p A_0^4\sigma^2\left\{\begin{array}{l}\delta\left(-n+m\right)+\delta\left[\left(n+m\right)-\left(q+p\right)\right] \\ +\delta\left[\left(n+m\right)-\left(q-p\right)\right] \\ +\delta\left(n+m\right)+\delta\left[\left(n-m\right)-\left(q+p\right)\right] \\ +\delta\left[\left(n-m\right)-\left(q-p\right)\right] \\ +\delta\left(q-n\right)+\delta\left(q-p\right)+\delta\left(q+p\right)\end{array}\right\} \\ &=\frac{23}{3}N^3A_0^4\sigma^2, \end{aligned} \tag{30}$$

$$\begin{aligned} &\sum_n\sum_m\sum_q\sum_p A_0^4\sigma^4\left\{\begin{array}{l}3\delta\left(n-m\right)\delta(q+p)+3\delta\left(n-m\right)\delta(q-p) \\ +3\delta\left(n+m\right)\delta(q+n)+4\delta\left(p-m\right)\delta(q-n) \\ +3\delta\left(n+m\right)\delta(q-p)+2\delta\left(p+m\right)\delta(q-n)\end{array}\right\} \\ &=18N^2A_0^2\sigma^4, \end{aligned} \tag{31}$$

$$\begin{aligned} &\sum_n\sum_m\sum_q\sum_p \sigma^6\left\{\begin{array}{l}\delta\left(n-m\right)\delta(q+p)+\delta\left(n-m\right)\delta(q-p) \\ +\delta\left(m-p\right)\delta(q-n)+\delta\left(n+m\right)\delta(q+p) \\ +\delta\left(n+m\right)\delta(q-p)+\delta\left(n+m\right)\delta(q+p)\end{array}\right\} \\ &=6N^2\sigma^6. \end{aligned} \tag{32}$$

Therefore,

$$E\left[R_{zs}\left(\beta_0,\gamma_0\right)R_{zs}^{*}\left(\beta_0,\gamma_0\right)\right] = N^4A_0^6+\frac{23}{3}N^3A_0^4\sigma^2+18N^2A_0^2\sigma^4+6N^2\sigma^6. \quad (33)$$

REFERENCES

[1] C.-C. Chen and H. Andrews, "Target-motion-induced radar imaging," *IEEE Trans. Aerosp. Electron. Syst.*, vol. AES-16, no. 1, pp. 2–14, Jan. 1980.

[2] V. C. Chen and S. Qian, "Joint time-frequency transform for radar range-Doppler imaging," *IEEE Trans. Aerosp. Electron. Syst.*, vol. 34, no. 2, pp. 486–499, Apr. 1998.

[3] P. Cheng, X. Wang, J. Zhao, and J. Cheng, "A fast and accurate compressed sensing reconstruction algorithm for ISAR imaging," *IEEE Access*, vol. 7, pp. 157019–157026, 2019.

[4] Z. Ding, T. Zhang, Y. Li, G. Li, X. Dong, T. Zeng, and M. Ke, "A ship ISAR imaging algorithm based on generalized radon-Fourier transform with low SNR," *IEEE Trans. Geosci. Remote Sens.*, vol. 57, no. 9, pp. 6385–6396, Sep. 2019.

[5] L. Li, L. Yan, D. Li, H. Liu, and C. Zhang, "A novel ISAR imaging method for maneuvering target based on AM-QFM model under low SNR environment," *IEEE Access*, vol. 7, pp. 140499–140512, Oct. 2019.

[6] L. Du, H. Liu, Z. Bao, and M. Xing, "Radar HRRP target recognition based on higher order spectra," *IEEE Trans. Signal Process.*, vol. 53, no. 7, pp. 2359–2368, Jul. 2005.

[7] C. Benedek and M. Martorella, "ISAR image sequence based automatic target recognition by using a multi-frame marked point process model," in *Proc. IEEE Int. Geosci. Remote Sens. Symp.*, Jul. 2011, pp. 3791–3794.

[8] M. Xing, R. Wu, Y. Li, and Z. Bao, "New ISAR imaging algorithm based on modified Wigner–Ville distribution," *IET Radar, Sonar Navigat.*, vol. 3, no. 1, pp. 70–80, 2008.

[9] Y. Wang, J. Kang, and Y. Jiang, "ISAR imaging of maneuvering target based on the local polynomial wigner distribution and integrated high-order ambiguity function for cubic phase signal model," *IEEE J. Sel. Topics Appl. Earth Observ. Remote Sens.*, vol. 7, no. 7, pp. 2971–2991, Jul. 2014.

[10] X. Lv, M. Xing, S. Zhang, and Z. Bao, "Keystone transformation of the Wigner–Ville distribution for analysis of multicomponent LFM signals," *Signal Process.*, vol. 89, no. 5, pp. 791–806, May 2009.

[11] X. Lv, M. Xing, C. Wan, and S. Zhang, "ISAR imaging of maneuvering targets based on the range centroid Doppler technique," *IEEE Trans. Image Process.*, vol. 19, no. 1, pp. 141–153, Jan. 2010.

[12] X. Lv, G. Bi, C. Wan, and M. Xing, "Lv's distribution: Principle, implementation, properties, and performance," *IEEE Trans. Signal Process.*, vol. 59, no. 8, pp. 3576–3591, Aug. 2011.

[13] S. Luo, G. Bi, X. Lv, and F. Hu, "Performance analysis on lv distribution and its applications," *Digit. Signal Process.*, vol. 23, no. 3, pp. 797–807, May 2013.

[14] J. Zheng, H. Liu, and Q. H. Liu, "Parameterized centroid frequency-chirp rate distribution for LFM signal analysis and mechanisms of constant delay introduction," *IEEE Trans. Signal Process.*, vol. 65, no. 24, pp. 6435–6447, Dec. 2017.

[15] Y. Li, Z. Bao, M. Xing, and R. Wu, "Inverse synthetic aperture radar imaging of ship target with complex motion," *IET Radar, Sonar Navigat.*, vol. 2, no. 6, pp. 395–403, Dec. 2008.

[16] Y. Li, M. Xing, J. Su, Y. Quan, and Z. Bao, "A new algorithm of ISAR imaging for maneuvering targets with low SNR," *IEEE Trans. Aerosp. Electron. Syst.*, vol. 49, no. 1, pp. 543–557, Jan. 2013.

[17] J. Zheng, T. Su, W. Zhu, L. Zhang, Z. Liu, and Q. H. Liu, "ISAR imaging of nonuniformly rotating target based on a fast parameter estimation algorithm of cubic phase signal," *IEEE Trans. Geosci. Remote Sens.*, vol. 53, no. 9, pp. 4727–4740, Sep. 2015.

[18] T. J. Abatzoglou, "Fast maximum likelihood joint estimation of frequency and frequency rate," *IEEE Trans. Aerosp. Electron. Syst.*, vol. 22, no. 6, pp. 708–715, Nov. 1986.

[19] L. Wu, X. Wei, D. Yang, H. Wang, and X. Li, "ISAR imaging of targets with complex motion based on discrete chirp Fourier transform for cubic chirps," *IEEE Trans. Geosci. Remote Sens.*, vol. 50, no. 10, pp. 4201–4212, Oct. 2012.

[20] P. O'Shea, "A new technique for instantaneous frequency rate estimation," *IEEE Signal Process. Lett.*, vol. 9, no. 8, pp. 251–252, Aug. 2002.

[21] P. O'shea, "A fast algorithm for estimating the parameters of a quadratic FM signal," *IEEE Trans. Signal Process.*, vol. 52, no. 2, pp. 385–393, Feb. 2004.

[22] Y. Wang, B. Zhao, and J. Kang, "Asymptotic statistical performance of local polynomial Wigner distribution for the parameters estimation of cubic-phase signal with application in ISAR imaging of ship target," *IEEE J. Sel. Topics Appl. Earth Observ. Remote Sens.*, vol. 8, no. 3, pp. 1087–1098, Mar. 2015.

[23] J. Zheng, T. Su, W. Zhu, and Q. Huo Liu, "ISAR imaging of targets with complex motions based on the keystone time-chirp rate distribution," *IEEE Geosci. Remote Sens. Lett.*, vol. 11, no. 7, pp. 1275–1279, Jul. 2014.

[24] X. Bai, R. Tao, Z. Wang, and Y. Wang, "ISAR imaging of a ship target based on parameter estimation of multicomponent quadratic frequency modulated signals," *IEEE Trans. Geosci. Remote Sens.*, vol. 52, no. 2, pp. 1418–1429, Feb. 2014.

[25] J. Zheng, T. Su, L. Zhang, W. Zhu, and Q. H. Liu, "ISAR imaging of targets with complex motion based on the chirp rate–quadratic chirp rate distribution," *IEEE Trans. Geosci. Remote Sens.*, vol. 52, no. 11, pp. 7276–7289, Nov. 2014.

[26] Y. Li, T. Su, J. Zheng, and X. He, "ISAR imaging of targets with complex motions based on modified Lv's distribution for cubic phase signal," *IEEE J. Sel. Topics Appl. Earth Observ. Remote Sens.*, vol. 8, no. 10, pp. 4775–4784, Oct. 2015.

[27] L. Yanyan, S. Tao, and Z. Jibin, "Inverse synthetic aperture radar imaging of targets with complex motions based on modified chirp rate–quadratic chirp rate distribution for cubic phase signal," *J. Appl. Remote Sens.*, vol. 9, no. 1, Dec. 2015, Art. no. 095036.

[28] J. Zheng, H. Liu, G. Liao, T. Su, Z. Liu, and Q. H. Liu, "ISAR imaging of nonuniformly rotating targets based on generalized decoupling technique," *IEEE J. Sel. Topics Appl. Earth Observ. Remote Sens.*, vol. 9, no. 1, pp. 520–532, Jan. 2016.

[29] D. Li, X. Gui, H. Liu, J. Su, and H. Xiong, "An ISAR imaging algorithm for maneuvering targets with low SNR based on parameter estimation of multicomponent quadratic FM signals and nonuniform FFT," *IEEE J. Sel. Topics Appl. Earth Observ. Remote Sens.*, vol. 9, no. 12, pp. 5688–5702, Dec. 2016.

[30] J. Zhang, Y. Li, T. Su, and X. He, "Quadratic FM signal detection and parameter estimation using coherently integrated trilinear autocorrelation function," *IEEE Trans. Signal Process.*, vol. 68, pp. 621–633, Jan. 2020.

[31] B. D. Carlson, E. D. Evans, and S. L. Wilson, "Search radar detection and track with the Hough transform. I. System concept," *IEEE Trans. Aerosp. Electron. Syst.*, vol. 30, no. 1, pp. 102–108, Jan. 1994.

[32] B. D. Carlson, E. D. Evans, and S. L. Wilson, "Search radar detection and track with the Hough transform. II. Detection statistics," *IEEE Trans. Aerosp. Electron. Syst.*, vol. 30, no. 1, pp. 109–115, Jan. 1994.

[33] B. Ristic and B. Boashash, "Comments on' the Cramer-Rao lower bounds for signals with constant amplitude and polynomial phase," *IEEE Trans. Signal Process.*, vol. 46, no. 6, pp. 1708–1709, Jun. 1998.

[34] D. Zhu, Y. Li, and Z. Zhu, "A keystone transform without interpolation for SAR ground moving-target imaging," *IEEE Geosci. Remote Sens. Lett.*, vol. 4, no. 1, pp. 18–22, Jan. 2007.

[35] Q. H. Liu and N. Nguyen, "An accurate algorithm for nonuniform fast Fourier transforms (NUFFT's)," *IEEE Microw. Guided Wave Lett.*, vol. 8, no. 1, pp. 18–20, Jan. 1998.

YANYAN LI received the M.S. and Ph.D. degrees in signal and information processing from Xidian University, Xi'an, China, in 2011 and 2016, respectively.

Since 2016, she has been a Lecturer with the School of Information Science and Technology, Northwest University. Her research interests include ISAR imaging, target detection, and time-frequency analysis.

JIANCHENG ZHANG received the M.S. and Ph.D. degrees from Xidian University, Xi'an, China, in 2011 and 2017, respectively.

His research interests include maneuvering target detection, parameter estimation, and time-frequency analysis.

JIBIN ZHENG (Member, IEEE) received the B.S. degree in electronic information science and technology from Shandong Normal University, Jinan, China, in 2009, and the Ph.D. degree in signal and information processing from Xidian University, Xi'an, China, in 2015.

From 2012 to 2014, he was a Visiting Ph.D. Student at the Department of Electrical Engineering, Duke University, Durham, NC, USA, through the financial support from the China Scholarship Council. Since 2015, he has been a Faculty Member of the National Laboratory of Radar Signal Processing, Xidian University, where he is currently an Associate Professor. His research interests include synthetic aperture radars (SAR) and inverse SAR signal processing, cognitive radars, time-frequency analysis, sparse Bayes learning, and KA-clutter suppression.

JINPING NIU received the Ph. D degree from Xidian University, Xi'an, China, in 2014.

She is currently an Associate Professor with the School of Information Science and Technology, Northwest University, Xi'an. Her research interests include signal processing and resource allocation for wireless communication systems.

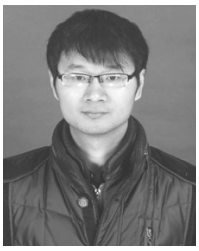

YAN ZHOU (Member, IEEE) received the Ph.D. degree from Xidian University, Xi'an, China, in 2015.

He is currently a Lecturer with the School of Information Science and Technology, Northwest University. His research interests include space-time adaptive processing and array signal processing.

NA MENG is currently pursuing the Ph.D. degree in information and communication engineering with Northwestern Polytechnical University.

She is a Lecturer with the School of Information Science and Technology, Northwest University. Her research interests include underwater target detection and recognition.